



**HAL**  
open science

## Experimental investigation of the brittle-viscous transition in mafic rocks – Interplay between fracturing, reaction, and viscous deformation

Sina Marti, Holger Stünitz, Renée Heilbronner, Oliver Plumper, Martyn Drury

### ► To cite this version:

Sina Marti, Holger Stünitz, Renée Heilbronner, Oliver Plumper, Martyn Drury. Experimental investigation of the brittle-viscous transition in mafic rocks – Interplay between fracturing, reaction, and viscous deformation. *Journal of Structural Geology*, 2017, 105, pp.62-79. 10.1016/j.jsg.2017.10.011 . insu-01636815

**HAL Id: insu-01636815**

**<https://insu.hal.science/insu-01636815v1>**

Submitted on 28 Nov 2019

**HAL** is a multi-disciplinary open access archive for the deposit and dissemination of scientific research documents, whether they are published or not. The documents may come from teaching and research institutions in France or abroad, or from public or private research centers.

L'archive ouverte pluridisciplinaire **HAL**, est destinée au dépôt et à la diffusion de documents scientifiques de niveau recherche, publiés ou non, émanant des établissements d'enseignement et de recherche français ou étrangers, des laboratoires publics ou privés.

1 **Experimental investigation of the brittle-viscous transition in mafic rocks –**  
2 **interplay between fracturing, reaction, and viscous deformation**

3

4 *\*Sina Marti<sup>a</sup>, Holger Stünitz<sup>b,c</sup>, Renée Heilbronner<sup>a</sup>, Oliver Plümper<sup>d</sup>, Martyn*  
5 *Drury<sup>d</sup>*

6 <sup>a</sup> Department of Environmental Sciences, Basel University, Switzerland  
7 (sina.marti@unibas.ch, +41 79 505 81 82, Brombacherstr. 27, 4057 Basel;  
8 renee.heilbronner@unibas.ch)

9 <sup>b</sup> Department of Geosciences, UiT the arctic University of Norway, Norway  
10 (holger.stunitz@uit.no)

11 <sup>c</sup> Institut des Sciences de la Terre d'Orléans (ISTO), Université d'Orléans, France

12 <sup>d</sup> Department of Earth Sciences, Utrecht University, Netherlands (O.Plumper@uu.nl;  
13 M.R.Drury@uu.nl)

14

15 **Keywords:** Rock deformation experiments, Brittle-viscous transition, Dissolution-  
16 precipitation, grain boundary sliding, Polyphase rheology

17

18 **Abstract**

19 Rock deformation experiments are performed on fault gouge fabricated from  
20 'Maryland Diabase' rock powder to investigate the transition from dominant brittle  
21 to dominant viscous behaviour. At the imposed strain rates of  $\dot{\gamma} \sim 3 \cdot 10^{-5} - 3 \cdot 10^{-6} \text{ s}^{-1}$ ,  
22 the transition is observed in the temperature range of ( $600 \text{ }^\circ\text{C} < T < 800 \text{ }^\circ\text{C}$ ) at  
23 confining pressures of ( $0.5 \text{ GPa} \leq P_c \leq 1.5 \text{ GPa}$ ). From microstructural observations,  
24 the transition is effected by a switch from brittle fracturing and cataclastic flow, to  
25 viscous dissolution-precipitation creep and grain boundary sliding. Mineral  
26 reactions and resulting grain size refinement by nucleation are observed to be  
27 critical processes for the switch to viscous deformation, i.e., grain size sensitive  
28 creep. In the transitional regime, the mechanical response of the sample is a mixed-  
29 mode between brittle and viscous rheology and microstructures associated with  
30 both brittle and viscous deformation are observed. As grain size reduction by  
31 reaction and nucleation is a time dependent process, the brittle-viscous transition is  
32 not only a function of T but to a large extent also of microstructural evolution.

33

## 34 **1. Introduction**

35 Our knowledge about rock strength is largely based on laboratory-derived data.  
36 Given the condition that the strength of the lithosphere cannot be greater than that  
37 of the constituting rocks and minerals, strength envelopes are constructed, which plot  
38 laboratory-derived strength or flow laws for minerals (or rocks) versus depth (as a  
39 proxy for pressure and temperature) (e.g. Brace and Kohlstedt, 1980; Kohlstedt et  
40 al., 1995; Burov, 2011 and references therein). Following the general consensus  
41 that the upper crust deforms dominantly by fracturing and the lower crust and  
42 upper mantle by viscous creep, the early strength envelopes were constructed  
43 using a constant strain rate, two-mechanism model (e.g., Brace and Kohlstedt,  
44 1980). Frictional rock strength (Byerlee, 1978) is plotted against depth to  
45 temperature and pressure conditions, where viscous deformation takes place at  
46 lower stresses than frictional sliding. Here, the term 'viscous' refers to temperature and  
47 rate sensitive deformation mechanisms such as dislocation and diffusion creep (including  
48 pressure solution creep).

49 Rocks deforming in the brittle field change their mode of deformation from frictional  
50 sliding along a discrete plane to distributed cracking at elevated pressures (e.g. Karman,  
51 1911; Kirby and Kronenberg, 1984), because frictional sliding at elevated confining  
52 pressures requires higher stresses than those needed to form new cracks. This change  
53 from discrete to distributed ('ductile') deformation mode is termed "brittle-ductile  
54 transition" (BDT) and is also termed the region of semi-brittle deformation (e.g. Kohlstedt  
55 et al., 1995). Towards greater depth, the semi-brittle field is terminated by another  
56 transition, which is primarily temperature dependent. This transition is termed the  
57 "brittle-plastic transition", where the term 'plastic' denotes a permanent, non-brittle  
58 deformation without specifying a particular mechanism (Kohlstedt et al. 1995). The term  
59 "plastic" may have different meanings in terms of rheology and deformation processes, so  
60 that the for a general temperature- and rate sensitive, pressure-insensitive deformation  
61 the more general term 'brittle-viscous' transition (BVT) is preferred and will be used in  
62 this text. The introduction of a semi-brittle field to the classical strength envelope predicts  
63 a broad transitional field from dominant brittle to dominant viscous deformation.

64 The onset of viscous deformation (BVT, or, alternatively, an increasing  $\alpha$ -factor for the  
65 effective pore pressure law at the BDT, according to Hirth and Beeler, 2015) within the  
66 Earth's crust is generally associated with the disappearance of earthquake rupture. Where  
67 the occurrence of the BVT is considered to be a simple function of pressure and  
68 temperature (as proxies for depth), the BVT regime may be considered as the lower depth

69 limit of the seismogenic zone (e.g. Sibson, 1982, 1984). However, at the BVT several  
70 processes are competing: fracturing, frictional sliding, crystal plasticity, and diffusive  
71 mass transfer. Given the number of parameters controlling the deformation, the  
72 BVT, where both, time-dependent viscous mechanisms and relatively more time-  
73 independent brittle and frictional processes significantly contribute to the  
74 deformation, is a complex system where temperature, pressure, fluid availability,  
75 grain size, strain rate, microstructure, rock composition (i.e. mineral assemblage),  
76 and chemical environment control the rheology. As a consequence, it is not  
77 surprising that there is a lack of laboratory data characterising the BVT in detail,  
78 despite pioneering seminal works by, e.g., e.g., Griggs et al. (1960); Heard (1960);  
79 Handin (1966); Byerlee (1967, 1968); Tullis and Yund (1977); Brace and Kohlstedt  
80 (1980); Carter and Tsenn (1987); and review in Paterson and Wong (2005) and references  
81 therein.

82 In the absence of flow laws for other crustal minerals, the viscous strength of the  
83 continental crust was first estimated using a dislocation creep flow law for quartz  
84 (Brace and Kohlstedt, 1980). However, large proportions of the lower continental  
85 crust, and most of the oceanic crust are of mafic composition and quartz is virtually  
86 absent. Strength estimates for these crustal parts could only be assessed since flow  
87 law parameters for plagioclase and pyroxene became available (e.g. Mackwell,  
88 1991; Raterron and Jaoul, 1991; Bystricky and Mackwell, 2001; Rybacki and  
89 Dresen, 2000; Rybacki et al., 2006; Chen et al., 2006; Dimanov et al., 2003;  
90 Dimanov and Dresen, 2005; Dimanov et al., 2007). Most of the data, however, is  
91 applicable to high temperature deformation, and experimental studies for mafic  
92 rocks at lower temperatures are scarce (e.g. Kronenberg and Shelton, 1980;  
93 Shelton et al., 1981; Rutter et al., 1985; Hacker and Christire, 1991; Tullis and  
94 Yund, 1987; Getsinger and Hirth, 2014).

95 One important aspect of the BVT - not represented in the strength envelope plots -  
96 is the development of the rheology of sheared rock over time or during a strain  
97 history. Fault- and shear zones may show a strain-dependent microstructural  
98 evolution, which, in turn, may cause a strain-dependent strength evolution. One of  
99 the consequences of such a strain-history-dependent evolution is that fault/shear  
100 zones are unlikely to initiate with their final steady state strength. It is frequently  
101 seen from natural examples that brittle and viscous deformation can occur

102 cyclically (e.g. Gratier et al., 2011; Price et al., 2012) or sequentially in time (e.g.  
103 Simpson, 1986; Fitz Gerald and Stünitz, 1993; Stünitz and Fitz Gerald, 1993;  
104 Trepmann and Stöckert, 2003; Mancktelow and Pennacchioni, 2005; Pennacchioni  
105 and Mancktelow, 2007; Fousseis and Handy, 2008; Goncalves et al., 2016; Bukovská  
106 et al., 2016).

107 Relatively little is known about the rheology of fault rocks undergoing the BVT. As  
108 fault zones are considered to sustain the highest differential stress values near the  
109 BVT, it constitutes a key regime controlling the dynamics of lithospheric fault-zone  
110 systems. In this study, we aim to further our understanding of the evolution and the  
111 rheology of mafic rocks at conditions where the rocks undergo their BVT. Significant  
112 amounts of the global seismic moment occur along faults within the oceanic crust  
113 and along subduction zones. A better understanding of the behaviour of mafic rocks  
114 at the BVT will potentially aid our understanding of earthquake distribution and  
115 seismic hazard in these regions.

116 Furthermore, in order to address the question of strain dependent rheology,  
117 experiments have been performed to various amounts of strain to observe  
118 microstructural changes and evolving mechanical properties during fault-/shear-  
119 zone formation. One of the aims of this study is to gain insights into the deformation  
120 processes active over the BVT in a mafic rock and how initiation and development  
121 of fault/shear zones are achieved. Mechanical response is measured and  
122 deformation mechanisms are identified in the brittle, the semi-brittle and the  
123 viscous field.

124

## 125 **2. Methods**

### 126 *2.1 Experimental procedure*

#### 127 *2.1.1 Sample material*

128 Experiments were performed on Maryland Diabase (Kronenberg and Shelton,  
129 1980). The Maryland Diabase starting material ([Table 1](#)) has a modal composition  
130 (by volume) of ~ Plagioclase (Pl): 57%, Clinopyroxene (Cpx): 32%, Orthopyroxene  
131 (Opx): 8%, accessories (Qz, Kfs, Ilm, Mag, Bt, Ap): 3% (mineral abbreviations after  
132 Whitney and Evans, 2010). The Pl shows a relatively homogeneous composition of  
133 ~ An<sub>65-70</sub> except for a thin rim with a lower Anorthite component of ~ An<sub>50-55</sub>. The  
134 core to rim area ratio is ~ 83 : 17 ( $\pm 3$ ). Some of the Cpx grains show a Mg-enriched

135 core. Pieces of Maryland diabase were crushed with a hand-press and  
136 subsequently crushed with an alumina hand-mortar. The resulting powder was  
137 dry-sieved to extract the desired grain size fraction  $\leq 125 \mu\text{m}$ .

138

### 139 *2.1.2 Experimental setup and sample assembly*

140 Experiments were performed using two modified Griggs-type deformation  
141 apparatus at the University of Tromsø, Norway, at confining pressures ( $P_c$ ) of  
142  $\sim 0.5, 1.0$  and  $1.5 \text{ GPa}$ , at temperatures ( $T$ ) of  $300, 500, 600, 700$  and  $800 \text{ }^\circ\text{C}$  and  
143 with constant displacement rates of  $\sim 10^{-8}$  to  $10^{-9} \text{ m s}^{-1}$  (resulting in strain rates of  
144  $\sim 3 \cdot 10^{-5}$  to  $3 \cdot 10^{-6} \text{ s}^{-1}$  for homogeneous sample deformation). See [Table 2](#) for a list  
145 of experiments and conditions.

146 The sample assembly is shown in [Figure 1](#). Solid salt is used as confining medium.  
147 Inner salt pieces are fabricated from potassium iodide (KI) for experiments at  $T \leq$   
148  $600 \text{ }^\circ\text{C}$  and sodium chlorite (NaCl) for experiments at  $T \geq 700 \text{ }^\circ\text{C}$ . KI is mechanically  
149 weaker than NaCl but shows partial melting at  $T > 600 \text{ }^\circ\text{C}$  at the pressures of the  
150 experiments, which is to be avoided. Outer salt pieces are always fabricated from  
151 NaCl.

152 The sample consist of a thin layer of crushed rock, produced by placing  $0.11 \text{ g}$  of  
153 MD powder +  $0.2 \mu\text{l H}_2\text{O}$  (equals  $0.18 \text{ wt.}\%$ ) between the  $\text{Al}_2\text{O}_3$  forcing blocks along  
154 a  $45^\circ$  pre-cut ([Figure 1](#)). Forcing blocks are cylindrical with a diameter of  $6.33 \text{ mm}$ .  
155 The sample and forcing blocks are placed in a weld-sealed platinum jacket  
156 ( $0.15 \text{ mm}$  wall thickness) with a  $0.025 \text{ mm}$  nickel foil insert. The amount of added  
157 water was chosen such that sufficient water is present for solution mass transport  
158 processes and mineral reactions, while not inducing mechanical pore pressure  
159 effects. No pore pressure effects in the presence of an aqueous fluid were inferred  
160 for contents up to  $0.5 \text{ wt } \% \text{ H}_2\text{O}$  by Kronenberg and Tullis (1984) and up to  
161  $0.3 \text{ wt}\% \text{ H}_2\text{O}$  by Negrini et al. (2013).

162 During the experiments, approximately  $84\%$  of the inelastic axial displacement is  
163 accommodated by a shear displacement along the piston-sample interface and  
164 approximately  $16\%$  by plane strain thinning of the shear zone. The initial shear  
165 zone thickness is calculated from the amount of Maryland diabase powder used,  
166 the final thickness is measured on thin sections prepared from the samples after  
167 the experiment ([Table 2](#)). The shear zone thickness is assumed to decrease linearly

168 throughout the experiment with increasing piston displacement.  
169 At higher temperatures, the coupling between forcing blocks and rock material in  
170 our experiments was found to be poor. Thus, 800 °C experiments were performed  
171 using forcing blocks with 6 regularly spaced grooves, ~ 300 µm wide and 150 µm  
172 deep, cut into the surface of both, the upper and lower forcing block.  
173 To bring a sample to the desired Pc -T conditions, the  $\sigma_1$ - and  $\sigma_3$ -pistons (Figure  
174 1) are advanced in small increments, alternated with increments of heating,  
175 Heating is achieved using a graphite resistance furnace and T is measured with a K-  
176 type thermocouple positioned adjacent to the centre of the shear zone (Figure 1).  
177 When the desired conditions are reached (after 5 to 8 h, duration is longer for  
178 higher Pc experiments), shear zone thickness is at ~ 0.83 mm. During the  
179 experiment, only the  $\sigma_1$ -piston is advanced. At the end of the experiment, samples  
180 are quenched to 200 °C within 2 minutes while simultaneously retreating the  $\sigma_1$ -  
181 piston to remove the load on the sample. After that, samples are brought back to  
182 room conditions by slowly removing the remaining load, temperature and Pc,  
183 during ~ 3 h.

184

## 185 *2.2 Derivation of stresses and strains*

### 186 *2.2.1 Data recording and processing*

187 During the experiment, the confining pressure, axial load, and displacement are  
188 recorded using a digital data-logging system (LabView, 7.1) at a sampling  
189 frequency of 1 Hz and temperature is monitored using a proportional integral  
190 derivative (PID) controller (Eurotherm) attached to the thermocouple.

191 Temperature is held within  $\pm 1$  °C by the controller. There is a vertical T gradient in  
192 the sample from the center outwards, ranging from ~ 17 °C/mm at 600 °C (Pec,  
193 2014).

194 The principal stress  $\sigma_3$  is considered to be equal to Pc (Eq. 1a), and  $\sigma_1$  is derived  
195 from the measured axial force per sample area.

$$196 \quad \sigma_3 = Pc \quad (1a)$$

$$197 \quad \Delta\sigma = \sigma_1 - \sigma_3 \quad (1b)$$

198

199  $\Delta\sigma$  is corrected for the decreasing overlap of the forcing blocks (i.e. decreasing

200 sample area) using a cosine-square approximation to the ACF.

201

$$202 \quad ac(i) = \cos^2 ( 90^\circ \cdot sd(i) / L) \quad (2a)$$

$$203 \quad \Delta\sigma_{AC} = ac \cdot \Delta\sigma \quad (2b)$$

204

205 where  $ac(i)$ : relative overlap of the forcing blocks;  $sd(i)$ : shear displacement  
206 parallel to the forcing block - sample interface;  $L$ : maximum possible shear  
207 displacement = diameter of forcing blocks (6.33 mm) /  $\cos(45^\circ)$  = 8.95 mm.

208

209 The shear and normal stresses,  $\tau$  and  $\sigma_n$ , supported by the sample inclined at  $45^\circ$   
210 are obtained by Mohr circle construction from  $\Delta\sigma_{AC}$ . The effective pore fluid  
211 pressures in our experiments is assumed to be negligible, i.e. is taken as zero.

212 Axial displacement is corrected for apparatus stiffness. Advancing the  $\sigma_1$ -piston  
213 leads to an increased Pc as a function of the compressibility of the confining  
214 medium. The correction is outlined in Richter et al. (2016). Differential stress with  
215 the solid salt assemblage in the Griggs rig are usually considered to overestimate  
216 rock strength eventually up to 100 MPa (e.g. Green & Borch, 1989).

217

## 218 *2.3 Analytical methods*

### 219 *2.3.1 Microscopy*

220 After the experiments, samples are impregnated with epoxy, cut parallel to the  
221 shear direction (in some cases also normal to it), and prepared to doubly polished  
222 thin sections. Optical light microscope, scanning electron microscope (SEM) and  
223 transmission electron microscope (TEM) are used for sample analysis. SEM  
224 analyses are performed either with the Zeiss Merlin SEM at Tromsø University, or  
225 with a Philips XL30 ESEM at the centre of microscopy (SNI) at Basel University.  
226 Chemical analyses are performed using energy dispersive X-ray Spectroscopy  
227 (EDS), at 15 kV acceleration voltage and using a ZAF matrix correction.

228

229 *Transmission electron microscopy (TEM)* analyses are carried out at Utrecht  
230 University using a FEI Talos 200FX equipped with a high-sensitivity Super-EDX  
231 system. TEM images are recorded in bright field (BF), high angular annual dark  
232 field (HAADF) and bright field scanning TEM (BF-STEM) modes. BF images are



233 highly sensitive on crystallographic orientation, whereas contrasts in HAADF  
234 images are sensitive to average atomic number (Z-contrast) of the material.

235

236 *Focussed ion beam (FIB)* foils for TEM investigations are prepared in a FEI Helios  
237 NanoLab 3G. The FIB foil of the 600 °C experiment is cut perpendicular to both the  
238 shear direction and the shear plane. The FIB foils of the 700 and 800 °C  
239 experiments are cut parallel to the shear direction and normal to the shear plane.

240

### 241 *2.3.2 Image analysis*

242 In this paper, micrographs are always oriented with the shear zone boundaries  
243 horizontal and with a dextral sense of shear. The reference coordinate system is  
244 shown in [Figure 2](#).

245

246 *FFT analyses of HR-TEM images:* In high-resolution (HR) TEM images where lattice  
247 planes of individual crystals are resolved, Fast Fourier Transformations (FFT) can  
248 be used to obtain the reciprocal space information akin to a direct diffraction  
249 pattern. Lattice fringes are only revealed when the crystal satisfies the diffraction  
250 condition. One single HRTEM image of a polycrystalline sample is not likely to  
251 reveal lattice fringes in all crystals. Therefore, FFT analysis used to detect  
252 diffractions on three HR-TEM images from the same area, with different tilt angles.

253

254 *EDS profiles:* Element concentrations along a line-profile are prepared using the  
255 software Fiji (<https://fiji.sc/>). A line-profile of 10 px width is defined, where the  
256 value at each point along the profile is an average over these 10 px. In this manner,  
257 the noise is reduced. The values are then normalized to the maximum count value  
258 (from the whole EDS map) of each element.

259

260 *Phase Segmentation:* Mineral phase segmentations are performed on BSE contrast  
261 SEM images. Phases are differentiated by their different Z-contrast using grey-level  
262 slicing. As Pyroxene (Px), Amphibole (Amph) and Zoisite (Zo) have similar Z-  
263 contrasts, manual post-processing is necessary to properly segment these phases.

264 *Shape and orientation of shear bands:* Shear bands and larger shear fractures are  
265 digitized manually on BSE contrast SEM images. The x-y coordinates of the outlines

266 are measured, smoothed (to remove digitizing artefacts) and exported using the  
267 program Fiji and analysed with the SURFOR program (Panozzo Heilbronner, 1984;  
268 Heilbronner and Barrett, 2014). The SURFOR results yield an orientation  
269 distribution function (ODF) of boundary segments of the analysed structures and  
270 is presented as a rose diagram. Shear band thicknesses were determined by  
271 dividing the digitized shear bands into approximately straight segments, using Fiji  
272 to extract the best fit ellipse of each segment and using the short axis of the ellipses  
273 as proxy for the shear band thickness.

274 *Grain size and shape:* Grain boundaries are traced manually on SE- and BSE- SEM  
275 images or on BF TEM images. The resulting grain maps are analysed with Fiji to  
276 derive the grain areas and the x-y coordinates of grain boundaries. The area  
277 equivalent diameters are calculated and grain size distributions are presented as  
278 histograms of equivalent diameters ( $d_{\text{equ}}$ ). Using a kernel density estimate  
279 (MATLAB function 'ksdensity'), the mode of the distribution is determined. Grain  
280 shape analyses are performed using the SURFOR program.

281

### 282 **3. Results**

283 Samples at  $T \leq 600$  °C develop similar microstructures and we therefore focus in  
284 this paper on the evolution from 600 – 800 °C. Reference frames of image  
285 orientation and angles are explained in [Figure 2a, b](#); terminology used when  
286 describing stress-strain curves is shown in [Figure 2c](#). Shear strain is always given  
287 as apparent shear strain  $\gamma_a$  (for calculation, see Appendix).

288

#### 289 *3.1 Mechanical data*

##### 290 *3.1.1 Stress-strain curves*

291 Shear stress vs. apparent shear strain curves are shown for T of 600 °C, 700 °C and  
292 800 °C and  $P_c$  of 0.5, 1.0 and 1.5 GPa ([Figure 3a](#)). Samples at 600 and 700 °C show a  
293 positive dependence of  $\tau$  on  $P_c$  between 0.5 and 1.0 GPa.

294 The comparison of the stress-strain data for 700 °C experiments between 1.0 and  
295 1.5 GPa  $P_c$  shows that the yield point occurs at relatively similar values. The 1.5  
296 GPa  $P_c$  experiments however, unlike all other experiments, show hardening at 700  
297 °C until  $\gamma_a \sim 2.3$  where stresses stay at approximately constant levels thereafter.

298 At 800 °C, sample strength is significantly lower than in lower T experiments and  
 299 within the variability between individual runs, no strength dependence on Pc is  
 300 detected. 800 °C experiments show a gradual weakening after peak stress and  
 301 reach a quasi-steady state at a  $\gamma_a \sim 4$  onwards (Figure 3a). Note also the lower  
 302 slope of the initial loading part of the stress-strain curve at 800 °C compared to  
 303 lower T experiments. Samples at 800 °C deform at stresses below the Goetze  
 304 criterion (the condition of  $\Delta \sigma = Pc$ , which is taken as the upper  $\Delta \sigma$ -limit of  
 305 plastic or viscous deformation; Kohlstedt, 1995. In our samples, which are oriented  
 306 at 45° to  $\sigma_1$ ,  $\Delta \sigma = 2 \cdot \tau$ ). At lower temperatures, all sample deform at  $\Delta \sigma$   
 307 clearly above the Goetze criterion.

308

### 309 3.1.2 Mohr Circle construction

310 From Mohr circle constructions (Figure 3b), the positive pressure dependence of  
 311 strength at 600 °C is clearly visible. Apparent friction coefficients ( $\mu'$ ) derived from  
 312 the Mohr circles yield a value of  $\mu' = 0.44$ . Experiments at 600 °C and 700 °C, 0.5  
 313 GPa Pc reach Byerlee's relationship (Byerlee, 1978) at 'yield', whereas at 1.0 GPa,  
 314 the stresses at both 'yield' and flow stay below it. At  $Pc \geq 1.0$  GPa, and  $T \geq 700$  °C,  
 315 shear stresses are pressure insensitive with an apparent friction coefficient of  $\mu' =$   
 316 0.05 at 700 °C. No " $\mu$ " was determined for 800 °C experiments, due to the  
 317 variability in the stress values and the sensitivity of the fitted " $\mu$ " to low slopes.  
 318 However, whereas 'yield' stresses do not show any significant pressure  
 319 dependence, quasi-steady state values reach lower values in the lower Pc  
 320 experiments at 800 °C.

321

### 322 3.1.3 Stress exponents

323 Combining constant displacement rate and displacement rate stepping tests, a  
 324 stress exponent  $n$  is determined as

325

$$326 \quad \tau \propto \dot{\gamma}^{1/n} \quad (3)$$

327

328 where  $\tau$ : shear stress and  $\dot{\gamma}$ : shear strain rate. To assess the influence of different  
 329 data correction routines on calculated stress exponents  $n$ , some of our data is

330 calculated with different published correction routines, to show their influence on  
331 the determined stress exponents. The corrections compared are:

332 1) 'R16': Data correction described in Richter et al. (2016). The same procedure for  
333 stress calculations is followed in this paper .

334 2) 'R16 + H&K10': Data correction after Richter et al. (2016) with the stress  
335 correction for the solid-salt assembly after Holyoke III and Kronenberg (2010).

336 3) 'P12': Data correction described in Pec et al. (2012).

337 4) 'P12 + H&K10': Data correction after (Pec et al., 2012) with the stress correction  
338 for the solid-salt assembly after (Holyoke III and Kronenberg, 2010).

339

340  $n$  values are determined for experiments performed at  $T = 300\text{ °C}$ ,  $P_c = 0.5\text{ GPa}$ ;  $T$   
341  $= 500\text{ °C}$ ,  $P_c = 1.0\text{ GPa}$ ;  $T = 700\text{ °C}$ ,  $P_c = 1.0\text{ GPa}$  and  $T = 800\text{ °C}$ ,  $P_c = 1.0\text{ GPa}$  (Figure  
342 4). For  $T \leq 500\text{ °C}$   $n$  is large with values  $> 19$ ,  $n$  for  $700\text{ °C}$  experiments is  
343 significantly lower with a value of 5.6 and  $n$  at  $800\text{ °C}$  is as low as 1.9. The  $n$  values  
344 determined from different data correction conventions from the literature vary by  
345 16 – 27% (Figure 4b). For example for the  $T = 800\text{ °C}$ ,  $P_c = 1.0\text{ GPa}$  experiments, a  
346 range of  $n$  values from 1.6 – 1.9 arises from different data treatment routines.

347

## 348 *3.2 Microstructures*

### 349 *3.2.1 Overview*

350 Strain in experiments at all  $P_c$ - $T$  conditions localizes into a network of shear  
351 fractures and/or shear bands. The term 'shear band' is used to refer to a zone (with  
352 a certain thickness) of high strain accumulation, without any implication of a  
353 specific deformation mechanism. As opposite to a 'shear fracture', which is  
354 accommodating displacement along a plane without any obvious distribution of  
355 strain within a volume (at SEM resolution).

356 The microstructures developed at different temperatures are systematically  
357 different (Figure 5). At  $600\text{ °C}$ , the microstructure is dominated by brittle  
358 deformation. Fracturing is extensive and a foliation (S), defined by elongated  
359 aggregate shapes, develops due to cataclastic flow (Figure 5a, b). Larger shear  
360 displacements are accommodated along shear fractures and shear bands, usually  
361 in Riedel shear ( $R_1$ ) orientation. Grain size reduction occurs via pervasive micro-  
362 fracturing (Figure 5b). No obvious strength difference between Pl and Px is

363 observed, as interpreted from the similar degree of fracturing and aggregate  
364 elongation of the two phases. In rare occasions, delicate pore trails are seen where  
365 fractures are partially healed, potentially indicating limited solution mass transfer  
366 (Figure 5c).

367 The microstructures in 700 °C experiments are discussed for the case of  $P_c = 1.0$   
368 and 1.5 GPa. At 700 °C, fracturing of (especially Px-) porphyroclasts is still  
369 observed and a weak foliation (defined by elongated aggregate shapes) forms  
370 partly by cataclastic flow (Figure 5d). Strain is localized in a network of thin (~ 5 –  
371 15  $\mu\text{m}$  wide) shear bands in  $C'$  orientations, cross-cutting the foliation (Figure 5d,  
372 e). These shear bands consist of small ( $\ll 1 \mu\text{m}$ ) grains of mainly Pl, Amph and Zo  
373 (Figure 5e). Amph and Zo are not part of the starting material and represent syn-  
374 kinematic reaction products. The reaction to Amph occurs preferentially along  
375 zones of localized deformation such as fractures within Px clasts and along shear  
376 bands (Figure 6). The reaction to Zo and more albitic Pl occurs throughout the  
377 samples, but small Zo needles predominantly occur in shear bands. Both, the Amph  
378 and Zo forming reactions are observed at  $P_c = 1.0$  and 1.5 GPa, but occur more  
379 extensively at 1.5 GPa.

380 At 800 °C broad shear bands form, separating low strain lenses between them  
381 (Figure 5f). Shear bands are recognized by small grain sizes and a fine-scale  
382 compositional layering defining a foliation (Figure 5g). Fracturing is only minor  
383 represented in the microstructure but can still be observed. Mineral reactions  
384 occur pervasively throughout the sample (i.e. are not restricted to high strain  
385 zones) but are more abundant in shear bands compared to low strain lenses. Amph  
386 either grows as coronas around Px grains or as aggregates within shear bands  
387 (Figure 5g) and has a composition between Mg-Hornblende to Tschermakite  
388 (Amph classification after Hawthorne et al., 2012). Zo grains occur as small needles  
389 within Pl clasts or within shear bands. Grain sizes in shear bands are usually  $< 1$   
390  $\mu\text{m}$ . Experiments at 800 °C and 1.5 GPa  $P_c$  show very similar microstructures but  
391 the Amph and especially Zo reaction are more abundant at the higher  $P_c$   
392 conditions.

393 Some melting is observed at 800 °C (melt vol.-% of total sample vol.  $\leq 2$ ), where the  
394 melt is mainly seen to form small pockets situated in extensional sites between  
395 larger porphyroclasts. No melt bands or shear-parallel melt layers are observed.

396 The geometry of strain localization changes over the temperature range from 600  
397 – 800 °C (Figure 7). Shear bands and shear fractures at 600 °C tend to be few, with  
398 large displacements. At 700 °C, shear bands are more abundant, shorter and more  
399 anastomosing compared to the lower T experiments. Fractures with larger  
400 displacements are less abundant but still observed. At 800 °C, shear bands are  
401 broad and form an anastomosing network. Generally no shear fractures with any  
402 significant amount of displacement are observed at 800 °C. The preferred  
403 orientations of shear bands and shear fractures with respect to the load axis  
404 increases from 30° at 600 °C (or 15° towards the shear zone boundaries) to 42° at  
405 800 °C (or 3° towards the shear zone boundaries; Figure 7).

406

### 407 *3.2.2 Shear bands formed in low T experiments*

408 Shear bands at 600 °C usually have a thickness of ~2 to 10 µm (Figure 7b) and  
409 occur both, along parts of the sample-forcing block interface and traversing the  
410 sample. The shear bands are either formed by ultra-cataclasites (type-I shear  
411 bands) or by a material that shows flow structures, seen by perturbation of a  
412 micron- to sub-micron scale compositional layering (type II shear bands) (Figure  
413 8a). There is a clear and relatively abrupt grain size gradient over a few microns  
414 from the lower strain areas into the type-II shear bands. Whereas the material in  
415 the low strain domains is usually pervasively fractured, no fractures or grain  
416 fragments are resolved within shear bands (at SEM resolution). A type II shear  
417 band as shown in Figure 8a has been studied in more detail by TEM. The material  
418 in the lower strain domains that border the shear bands consists of larger (>>100  
419 nm) angular Pl fragments and the boundary to the shear band material is sharp  
420 (Figure 8b). The shear band itself is composed of nano-crystalline and amorphous  
421 material in lenticular aggregates and layers, both with fairly sharp boundaries.  
422 Some crystals, identifiable by their darker appearance due to diffraction, are  
423 observed within the amorphous layers (Figure 8b - d). Lattice planes, seen in high-  
424 resolution BF HRTEM images and detected in FFT images show that the  
425 amorphously appearing layers still contain nano-crystals (Figure 8d).

426

### 427 *3.2.3 Shear bands formed in intermediate T experiments*

428 [Figure 9](#) presents microstructures from shear bands developed at 700°C, 1.0GPa  
429 Pc. At these 700 °C and Pc of 1.0 and 1.5 GPa conditions, shear bands are fully  
430 crystalline and mainly composed of fine-grained Pl and Amph ([Figure 9c](#)). Pl grain  
431 sizes are on the order of ~100 – 200 nm ([Figure 9b](#); [12](#)). [Figure 9e](#) shows the result  
432 of TEM EDS analysis over an area containing a small Pl porphyroclast surrounded  
433 by fine-grained Pl in the shear band. Plotting the relative amounts of the elements  
434 Si, Ca and Al along a profile from the porphyroclast into the fine-grained matrix  
435 shows slightly higher Al and Ca contents and lower Si content in the porphyroclast  
436 compared to the Pl within the shear band.

437

#### 438 *3.2.4 Shear bands formed in high T experiments*

439 Shear bands formed at 800 °C (Pc = 1.0 and 1.5 GPa) are fully crystalline. The  
440 typical microstructure shows fine-grained Pl interlayered with Amph (+Qz)  
441 ([Figure 10a, c](#)) and a close-up on the Pl grains shows ‘diamond shaped’, largely  
442 defect-free grains with a weak shape preferred orientation ([Figure 10b](#); [11](#)). The  
443 mean axial ratio of grains is  $b/a = 0.64$  and grain sizes are on the order of ~ 0.15 –  
444 0.50  $\mu\text{m}$  ([Figure 12](#)). Pore space along grain boundaries is almost absent and grain  
445 boundaries are tight ([Figure 10b](#); [11a](#)). Pl grain boundaries show a strong  
446 preferred orientation in two maxima ~ 10 – 30° away from the shear plane in both  
447 directions ([Figure 11](#)). Aligned grain boundaries are frequently observed, where  
448 relatively straight grain boundaries can be traced continuous over several  
449 neighbouring grains ([Figure 11c](#)). The ODF of grain boundary segments is weakly  
450 anisotropic with a monoclinic shape, consistent with the global dextral sense of  
451 shear.

452

#### 453 *3.2.5 Grain size distribution of plagioclase in shear bands formed in 700 – 800 °C* 454 *experiments*

455 [Figure 12](#) presents grain size distributions (GSD) measured from Pl grains within  
456 shear bands formed at 700 and 800 °C. Due to the small grain sizes in shear bands  
457 at 700 °C, it is difficult to distinguish individual grains. The best results were  
458 obtained from SE SEM images of broken surface as shown in [Figure 9b](#). For the 800  
459 °C experiments, grain maps were produced from both TEM and SEM images. Size  
460 distributions obtained from TEM and SEM images are similar and the GSD



461 presented in [Figure 12b](#) is measured on Pl grains from TEM images (similar to  
462 those shown in [Figure 10](#)). The GSD in [Figure 12a](#) is measured from grains  
463 segmented on SEM images of broken surfaces of a shear band top-view ([Figure 9b](#)),  
464 thus from a quasi-3D view, whereas the GSD in [Figure 12b](#) is from the 2D section of  
465 grains measured from a FIB foil in the TEM. Consequently, the two GSD are not  
466 fully comparable but yield a semi-quantitative measure of the grain size  
467 differences in shear bands between 700 and 800 °C experiments. The size  
468 distribution developed at 700 °C is narrow and > 80% of all grains are within 0.11  
469 – 0.25 µm. The mode of the calculated kernel density estimate fit lies at 0.17 µm.  
470 The GSD at 800 °C is somewhat broader and > 80% of all grains are within 0.15 –  
471 0.50 µm with a mode of the kernel density estimate calculated fit at 0.30 µm.

472

### 473 *3.2.6 Shear band evolution with strain in 800 °C experiments*

474 [Figure 13](#) presents the evolution of shear bands at 800°C, as observed from  
475 experiments performed to different amounts of bulk strain, from peak stress ( $\gamma_a \sim$   
476 0.7) to a max of  $\gamma_a \sim 6.8$ . At peak stress, initial shear localization occurs mainly  
477 along favourably oriented grain- and phase boundaries. These initial zones are  
478 short ( $\sim 100 - 200 \mu\text{m}$ ), distributed (not interconnected) and make an angle of  
479  $\sim 27^\circ$  with the load axis. From the microstructure it is apparent that these  
480 structures are often dilatant: minor melt segregations, microfracturing and  
481 nucleation of new grains/phases such as Amph and Pl are observed ([Figure 14](#)).  
482 With increasing strain, the initial shear bands start to connect by the formation of  
483 interconnected zones of fine-grained material. These zones make a smaller angle to  
484 the shear zone boundaries (or  $\sim 39^\circ$  with respect to the load axis) and have a  
485 width of  $\sim 10 - 20 \mu\text{m}$ . At a shear strain of  $\gamma_a \sim 4$ , a network of anastomosing  
486 shear bands has formed, with  $\sim 3^\circ$  with respect to the shear zone boundaries (i.e.  
487  $42^\circ$  to the load axis). The main shear band strand has a thickness of 50 – 150 µm.  
488 This microstructure coincides with the attainment of a quasi-steady state in the  
489 mechanical data ([Figure 13a, b](#)). With increasing strain, the vol.-% of shear bands  
490 increases. Irrespective, sample strength varies only slightly between  $\gamma_a \sim 4$  to 6.8  
491 despite the significant increase in vol.-% of shear bands ([Figure 13b, c](#)).

492



493 *3.2.7 Shear band orientation from peak stress to higher strains*

494 **Figure 15** shows the difference of shear band orientation at peak stress  
495 (~ coinciding with initiation of localization) and at higher strains (at quasi-steady  
496 state), as a function of temperature. Initial shear bands at all temperatures show  
497 the same preferred orientation, with 27° towards the load axis. This orientation  
498 stays relatively constant at ~ 30° in 600 °C experiment, but angles increase to 33°  
499 at 700 °C and 42° at 800 °C.

500

501 **4. Discussion**

502 The strains attained in our experiments are insufficient to attain full  
503 microstructural steady state. However, it is expected that the mechanical data  
504 reaches quasi-steady state values. The inferred rheology of the samples (e.g. as  
505 approximated by the determined stress exponents) always represents a bulk  
506 sample rheology, caused by combined mechanisms of deformation and their  
507 different rates in low strain domains and shear bands.

508

509 *4.1 Deformation mechanisms*

510 *4.1.1 low T experiments*

511 At 600 °C, displacement is mainly accommodated by cataclastic flow. The  
512 mechanical data shows a clear positive dependence of sample strength on  $P_c$   
513 (**Figure 3a, b**). High  $n$  values of ~20 (**Figure 4**) are in accordance with dominant  
514 brittle deformation and frictional sliding, as it is observed from the microstructure  
515 (**Figure 5b**). Some viscous component of deformation may be indicated by the fact  
516 that the  $n$  values are not as high as could be expected for purely frictional  
517 behaviour.

518 Displacement in 600 °C experiments is localized in a network of shear fractures  
519 and fine-grained shear bands (**Figure 5a, b; 7**), some of which contain amorphous  
520 material (**Figure 8**). The angles of shear bands and shear fractures to the load axis  
521 (~27° - 30°, **Figure 15**) are in accordance with brittle Riedel ( $R_1$ ) structures.

522 The area-% of shear bands in the thin section is about 1 – 2%. As an upper-bound  
523 estimate, if all displacement were to be accommodated by the shear bands, the  
524 strain rate  $\dot{\gamma}$  within them would be on the order of

525

526  $\dot{\gamma} = 10^{-5} \text{ mm s}^{-1} / (0.64 \text{ mm} \cdot 0.02) \approx 8 \cdot 10^{-4} \text{ s}^{-1}$  (3)

527

528 which is the applied displacement rate divided by 2% of the approximate shear  
529 zone thickness. Although the strain rate within the shear bands is likely to be high,  
530 it stays well below seismic rates.

531 Partly amorphous shear bands as we observe them during aseismic brittle faulting  
532 have previously been described (e.g. Yund et al., 1990; Goldsby and Tullis, 2002;  
533 Janssen et al., 2010; Pec et al., 2012, 2016). Our TEM analyses show that the shear  
534 bands consist of amorphous material, with layers and lenses of nano-crystalline  
535 material (Figure 8). A clear material difference is seen between Pl and Px, where Pl  
536 preferentially becomes amorphous and Px remains largely crystalline, with very  
537 small sizes (< 50 nm, Figure 8c). This is similar to the results of Pec et al. (2012,  
538 2016) or Yund et al. (1990): In their granitoid sample material amorphous shear  
539 bands form extensively within the feldspatic material.

540 The boundaries between shear bands and host rock in our samples are sharp, even  
541 on the nano-scale (Figure 8b). It appears from the microstructure that crystalline  
542 material is comminuted to a certain grain size (< 50 nm) and below that,  
543 amorphization (mainly of the Pl) is effective. (Pec et al., 2012, 2016) discuss  
544 different possible formation mechanism for their amorphous material and  
545 conclude that the most likely mechanism is a type of mechanical amorphization, i.e.  
546 high defect densities until crystallinity is lost. Feldspars appear to be particularly  
547 susceptible to this process, as also supported by this study. The rheology of these  
548 (partly-)amorphous shear bands, however remains yet unclear.

549

#### 550 *4.1.2 High T experiments*

551 At 800 °C, there is a significant difference in rheology compared to lower T  
552 experiments: differential stresses at 800 °C are half as high as at 700 °C and stay  
553 always below the Goetze criterion (Table 2; Figure 3a). Initial stress increase  
554 during sample loading (before peak stress) shows lower slopes at 800 °C (Figure  
555 3a), indicating a larger component of viscous deformation early in the experiment.  
556 The microstructure at 800 °C is dominated by mineral reactions and strong grain  
557 size refinement (Figure 5f, g; 10). The grain size within shear bands ranges mainly  
558 between 0.15 – 0.50 µm for Pl (Figure 12b), with similar sizes for Amph and Zo.

559 Grain size reduction takes place mainly by nucleation of new grains in conjunction  
560 with mineral reactions and potentially aided by strain energy reduction by  
561 replacing old, defect-rich porphyroclasts by new defect-free grains. The small grain  
562 sizes facilitate a grain size sensitive creep mechanism, where the strain rate is  
563 proportional to  $d^{-m}$  (e.g. Ashby and Verrall, 1973; Coble, 1963; Rutter, 1976), where  
564  $d$  is the grain size and  $m$  the grain size exponent. Diffusion creep and grain  
565 boundary sliding (GBS) are known to only leave few microstructural traces of their  
566 activity. However, aligned grain boundaries, equant to weakly anisotropic grain  
567 shapes, and low internal defect densities of grains are microstructures  
568 characteristic for GBS and diffusion creep (e.g. Elliott, 1973; Boullier and Gueguen,  
569 1975; Gifkins, 1976; Drury and Humphreys, 1988; Kilian et al., 2011; Drury et al.,  
570 2011). The shear bands consist of small, elongated hexagonal grains, whose grain  
571 boundaries can be contiguous over several grain diameters (Figure 11). The  
572 contiguous grain boundaries are well orientated for sliding in all orientations. As  
573 the experiments are performed with H<sub>2</sub>O present, dissolution-precipitation creep  
574 (DPC) is interpreted to be the dominant form of diffusion creep.  
575 DPC needs to be accommodated by some GBS (Lifshitz sliding of Langdon 2006),  
576 but the main strain contribution in very small sized aggregates may take place by  
577 GBS, where diffusive mass transport accommodates shape changes (Rachinger  
578 sliding of Langdon 2006). As both processes are closely linked and interconnected,  
579 the term DPC includes both, diffusion creep and GBS.  
580 DPC as a dominant deformation mechanism is in accordance with the low observed  
581 stress exponents of  $n \sim 1.9$ . Usually, stress exponents for diffusion creep are  
582 expected to be close or equal to 1 (e.g. Ashby and Verrall, 1973; Coble, 1963;  
583 Karato, 2008, Kohlstedt and Hansen, 2015; Paterson, 2013), but higher  $n$  values  
584 have been suggested for DPC, depending on the driving potentials or chemical  
585 potential gradients along the grain contact area (e.g., Gratier et al. 2009, 2013). In  
586 low strain domains grain sizes are large and DPC will not be an efficient  
587 deformation mechanism in these. Frictional sliding may be active in the low strain  
588 domains (but not dominant), increasing the stress exponent of the bulk sample to  $n$   
589 = 1.9. Diffusion creep as viscous deformation mechanism has previously been  
590 suggested for experimentally deformed basaltic material (under water added  
591 conditions) by e.g. Rutter et al. (1985); Getsinger and Hirth (2014), whereas Rutter

592 et al. (1985) state more in detail, that they interpret DPC together with GBS to be  
593 the dominant deformation mechanism.

594

#### 595 *4.1.3 Intermediate temperature experiments*

596 The microstructure at 700 °C shows characteristics of both DPC (including GBS)  
597 and cataclastic flow. Cataclastic flow thereby is mainly observed to contribute to  
598 deformation in low strain lenses (Figure 5d; 6). In shear bands, the similar  
599 microstructures as in shear bands at 800 °C suggest that DPC is the dominant  
600 deformation mechanisms in shear bands at 700 °C too. The main difference  
601 between 800 and 700 °C is the somewhat smaller grain sizes in shear bands at 700  
602 °C (Figure 12).

603 Fracturing at 700 °C is subordinate within shear bands. Fracturing and cataclasis  
604 are expected to produce a wide range of grain sizes with angular grain shapes (e.g.  
605 Stel, 1981; Storti et al., 2003; Keulen et al., 2007), unlike the observed  
606 microstructure. TEM-EDS mapping also reveals a compositional difference  
607 between Pl porphyroclast and fine-grained shear band Pl (Figure 9), which is  
608 further evidence that the plagioclase grains within the shear bands are not a result  
609 of fracturing but rather result from neocrystallization. The chemical differences are  
610 small but the coupled Al+Ca decrease with a Si increase from the clast to the shear  
611 band is consistent with a change towards lower anorthite content in the matrix Pl  
612 of the shear band. The measured change in Pl chemistry between porphyroclasts  
613 and fine-grained shear band Pl also excludes subgrain rotation recrystallization  
614 and instead points to nucleation as means of grain size reduction.

615 However, a brittle precursor to the shear bands at 700°C is possible, interpreted  
616 from the initiation of shear bands with the same low angle towards the load axis as  
617 in the brittle dominated 600°C experiments (Figure 15), as well as by the similar  
618 sample strengths for 600 and 700°C experiments. Due to the low strains at shear  
619 band initiation (~ at peak stress) it is, however, difficult to identify from the  
620 microstructure if and in which proportions viscous or brittle processes contribute  
621 at the point of initiating strain localization.

622 At 700 °C, sample strength as seen from the stress-strain curves is comparable to  
623 the 600 °C experiments (Figure 3a) with a significantly lower stress sensitivity on  
624 strain rate ( $1/n$ ) ( $n = 5.6$  at 700 °C,  $n > 19$  at  $T < 600$  °C; Figure 4a). The stress

625 exponent of 5.6 is just slightly higher than what would be typical for dislocation  
626 creep ( $n = 3$  to  $5$ ; Karato, 2008; Paterson, 2013; Kohlstedt and Hansen, 2015), but  
627 none of the microstructures indicate evidence for crystal plasticity. Rather, the  
628 intermediate  $n$ -value is interpreted to result from a combination of predominantly  
629 brittle ( $n$ -values of 19.5 and higher) and viscous processes ( $n \sim 1.9$ ), as it is  
630 observed in the microstructure.

631

#### 632 *4.1.4 Summary of deformation mechanisms*

633 The dominance of viscous deformation at 800 °C, and of brittle deformation at 600  
634 °C is evident, both from the mechanical data and the microstructure. Samples  
635 deformed at 700 °C are an intermediate case, where strain is localized into shear  
636 bands which are interpreted to deform with a viscous deformation mechanism but  
637 with stress-strain curves and strengths more like the brittle-dominated 600 °C  
638 samples (Figure 3a).

639 Shear bands formed in 700 °C experiments, like the shear bands at 800 °C, are  
640 interpreted to accommodate strain mainly by DPC and GBS. However, low strain  
641 lenses at 700 °C show abundant microfracturing and a contribution of cataclastic  
642 flow to deformation. The stress exponent is considerably lower at 700 °C than for  
643 lower T experiments (Figure 4a), indicating an increased viscous component to the  
644 rheology at 700 °C. The stress exponent of  $n = 5.6$  for 700 °C experiments is  
645 interpreted as a mixed mechanical response determined by the rheology of  
646 viscously deforming shear bands and partly frictional/cataclastic low strain lenses.  
647 The transition from dominantly brittle deformation to dominantly viscous flow in  
648 our experiments is seen to initiate with the dominance of solution-mass transport.  
649 Mineral reactions and nucleation lead to grain size reduction and thus strongly  
650 enhance the strain rate of grain size sensitive creep mechanisms. For our imposed  
651 experimental displacement rates, the transition occurs around 700 °C (although  
652 not fully  $P_c$  insensitive). In deformation experiments on whole-rock cores of  
653 Maryland Diabase at conditions similar to ours, Kronenberg and Shelton (1980)  
654 observed a brittle-viscous transition in their samples around 700 °C for a  $P_c = 1.0$   
655 GPa, comparable to our observations. However their strain rate was approximately  
656 one order of magnitude lower.

657 In our experiments, the influence of Pc is less pronounced compared to that of the  
658 temperature. Increasing the Pc at, e.g., 600 °C does not lead to a transition to more  
659 viscous behaviour. At 700 and 800 °C, the main effect of increasing the Pc is the  
660 formation of a higher abundance of reaction products. This indicates a rate-  
661 enhancing effect of increasing Pc on solution-mass transport processes and/or  
662 reaction kinetics, e.g., by a greater overstepping of reaction boundaries for  
663 pressure sensitive reactions.

664

## 665 *4.2 Microstructural evolution and its influence on bulk rheology*

### 666 *4.2.1 Shear band evolution*

667 As seen from 800 °C experiments, shear bands are widening and increase in vol.-%  
668 with increasing strain ([Figure 13](#)), caused by the on-going process of mineral  
669 reactions and nucleation, leading to the replacement of old, coarser-grained  
670 porphyroclasts by new, sub-micron sized grains. Shear band vol.-% stays relatively  
671 low in 700 °C experiments for the strains achieved, and interconnectivity is much  
672 lower than at 800°C (e.g. [Figure 7](#)). From the mechanical data it is seen that 700 °C  
673 experiments still show a large influence of brittle deformation, which is attributed  
674 to the low volume percentage, unfavourable orientation (not parallel to shear zone  
675 boundary but inclined against it with  $\sim 7^\circ$ ), and poor interconnectivity of shear  
676 bands. With increasing shear band widening, the viscous rheology of the shear  
677 bands at 700 °C is expected to eventually become more dominant.

678 As reaction and diffusion rates are lower at lower T, more time (or equivalently  
679 strain) is needed in the case of the 700 °C experiment to attain a connected  
680 network of shear bands as it is observed at 800 °C. However, the positive feedback  
681 between fracturing and reaction kinetics (as seen from extensive mineral reactions  
682 along microfractures in 700 °C experiments, [Figure 6](#)) aids the microstructural  
683 change, i.e. grain size reduction by reaction and nucleation, and appears to be an  
684 important mechanism in switching from dominant brittle to more viscous  
685 rheology.

686 Comparing the orientations of shear bands formed at different T ([Figure 7](#)) it is  
687 apparent that the orientations are less favourable for bulk shear displacement in  
688 600 and 700 °C compared to 800 °C experiments, due to the higher inclination of  
689 shear bands to the shear zone boundaries. Thus, shear band orientation is an

690 additional factor determining how the weak phase controls the rheology (cf. Gerbi  
691 et al., 2016).

692

693 *4.2.2. Shear band influence on bulk rheology in high-T experiments – estimating flow*  
694 *stresses in shear bands from plagioclase diffusion creep flow law*

695 The shear band evolution in 800 °C experiments shows an increasing dominance in  
696 shear band orientations (sub-)parallel to the shear zone boundaries (Figure 13)  
697 with increasing shear band widening and interconnection. That is, the shear band  
698 network evolves into geometrically more favourable orientations. Sample  
699 strengths, however, remain relatively high, with shear stress values of  $\tau > 190\text{MPa}$   
700 (Table 2; Figure 3a). Additionally, a quasi-steady state in the stress-strain curves at  
701  $\gamma_a \gtrsim 4$  is reached, disregarding a still increasing shear band vol.-%. These  
702 observations again suggest that the bulk sample rheology is not simply determined  
703 by the rheology of the shear bands.

704 For our experimental samples, the imposed displacement rate, temperature and  
705 the grain size within shear bands are known. At 800°C, where dissolution  
706 precipitation creep is interpreted to dominate the deformation, we can attempt to  
707 calculate expected stresses within shear bands for the given conditions. At present,  
708 however, the lack of, e.g., mineral solubility data and properties of grain boundary  
709 fluid films does not allow to calculate strain rates from common dissolution  
710 precipitation creep flow laws at the elevated Pc/T conditions of our experiments.  
711 We use a simplified approach to estimate the shear band rheology by applying the  
712 flow law of Rybacki and Dresen (2000) (shortened as ‘RD00’) for diffusion creep in  
713 feldspars, as has been done previously by e.g. Getsinger and Hirth (2014). The flow  
714 law of RD00 has the form:

715

$$716 \quad \dot{\epsilon} = A \cdot \Delta\sigma^n \cdot d^{-m} \cdot \exp\left(-\frac{Q}{RT}\right) \quad (5)$$

717

718 where  $A$  : constant,  $\Delta\sigma$  : differential stress,  $n$  : stress exponent (usually  $\sim 1$ ),  $d$  :  
719 grain size,  $m$  : grain size exponent,  $Q$  : activation energy,  $R$  : universal gas constant,  
720  $T$  : temperature.



721 Under the assumption that the shear bands accommodate the majority of the  
 722 deformation, a shear strain rate of  $\sim 1 \times 10^{-4} \text{ s}^{-1}$  is assumed for them. This is  
 723 derived from the imposed displacement rate,  $\sim 1 \times 10^{-5} \text{ mm s}^{-1}$  divided by the  
 724 cumulative shear band thickness,  $\sim 8 \times 10^{-2} \text{ mm}$  (which is 10 – 20% of the total  
 725 sample thickness at quasi-steady state in the mechanical data, e.g. [Figure 13](#)).  
 726 Using the RD00 flow law for diffusion creep in a wet plagioclase aggregate, we use  
 727 a strain rate of  $1 \times 10^{-4} \text{ s}^{-1}$ , a grain size range of 0.15 – 0.50  $\mu\text{m}$  and  $T = 800 \text{ }^\circ\text{C}$ . To  
 728 compare our shear strain rates to the axial shortening strain rates of the flow law,  
 729 the conversion from axial shortening to simple shear strain rates after Schmid et al.  
 730 (1987) is used, reformulating Eq. (5) to :

731

$$732 \quad \dot{\gamma} = A \cdot \sqrt{3}^{(n+1)} \cdot \tau^n \cdot d^{-m} \cdot \exp\left(-\frac{Q}{RT}\right) \quad (6)$$

733  $\dot{\gamma}$  : shear strain rate,  $A$ : constant,  $n$ : stress exponent = 1,  $\tau$  : shear stress,  $d$ : grain  
 734 size,  $m$ : grain size exponent = 3,  $Q$ : activation energy,  $R$ : universal gas constant,  $T$ :  
 735 temperature.

736

737 Solving Eq. (6) for shear stresses, they are calculated as:

$$738 \quad \tau = \exp\left(\log\left(\frac{\dot{\gamma}}{A \cdot \sqrt{3}^{(n+1)} \cdot d^{-m}}\right) - \left(\frac{-Q}{R \cdot T}\right)\right) \quad (7)$$

739

740 Resulting shear stresses are between 0.4 – 16 MPa. That is one to almost three  
 741 orders of magnitude lower than measured in the mechanical data. Conversely, if  
 742 Eq. (6) were used to calculate the strain rate for the given  $T$  and  $d$ , with the  
 743 measured  $\tau = 200 \text{ MPa}$ , strain rates of  $1 \times 10^{-3}$  to  $5 \times 10^{-2} \text{ s}^{-1}$  would result.

744 Our experimental samples contain higher wt.-%  $\text{H}_2\text{O}$  compared to the samples of  
 745 Rybacki and Dresen (2000), which is likely to have a marked effect on the rate of  
 746 DPC. Nonetheless, despite some uncertainties in the application of the RD00 flow  
 747 law, the results are expected to yield values within the expected order of  
 748 magnitude for DPC. The calculated stresses for the shear bands thus suggest that  
 749 the elevated bulk sample strengths of  $\tau \approx 200 \text{ MPa}$  at the given bulk strain rate of  
 750  $10^{-5} \text{ s}^{-1}$  cannot be explained by representing the fine-grained material within shear  
 751 bands. Rather, an effect by a load-bearing framework of low strain lenses due to



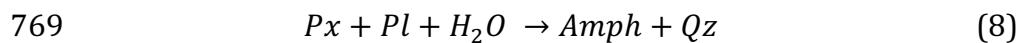
752 insufficient connectivity and unfavourable orientation of shear bands is suggested  
753 to explain the observed bulk sample strengths. Bulk sample strength is interpreted  
754 to be determined by the combined rate of DPC and GBS in the coarse-grained low  
755 strain lenses and the fine-grained shear bands. The onset of DPC does not depend  
756 on the occurrence of shear bands but because diffusion lengths are proportional to  
757 the grain size, the rate of strain accommodation by DPC will vary strongly between  
758 fine grained shear bands compared to low strain lenses which largely preserve the  
759 coarse initial grain sizes. Delocalized viscous processes prior to shear band  
760 formation are also indicated by the lower initial slope of the loading curve in the  
761 mechanical data ([Figure 3a](#)), indicating a more viscous component of sample  
762 deformation from the start of the experiment . DPC is speculated to cause this  
763 viscous relaxation.

764

#### 765 *4.2.3 The influence of strain on reaction rate as seen from the microstructure*

766 At 700 °C, fractures in Px porphyroclasts are extensively decorated by Amph  
767 overgrowths ([Figure 6](#)), where Amph is forming by the reaction:

768



770

771 Amph is seen to grow along Px-internal fractures with no contacting boundary  
772 towards Pl, indicating that element transport along the fractures occurred over  
773 several  $\mu\text{m}$  distance. It is described in the literature that fracturing can lead to high  
774 dislocation densities in the host crystal and is frequently associated with porosity  
775 (e.g. Fitz Gerald et al., 1991; Fitz Gerald and Stünitz, 1993; de Ronde et al., 2005).  
776 Fitz Gerald and Stünitz (1993) interpret from their observations that permeability  
777 along the microfractures must have been greatly enhanced, allowing for solution  
778 mass transport and mineral reactions along the fracture. Also from our  
779 observations, there is a clear positive feedback between deformation and reaction.  
780 This seems especially important in the 700 °C experiments, where the positive  
781 contribution of deformation on reaction rate is seen more strongly in the  
782 microstructure compared to 800 °C experiments. This is not unexpected, as  
783 reaction and diffusion rates will increase with increasing temperature and the

784 rate-enhancing effects of deformation on reaction and diffusion may become less  
785 important.

786

#### 787 *4.3 Linkage to natural faults*

788 The findings from our experiments suggest that a transition from brittle to viscous  
789 deformation in the studied mafic rock type initiates where solution-mass transport  
790 processes occur at sufficiently high rates to accommodate deformation at the  
791 imposed strain rate. No significant contribution of crystal plastic processes could  
792 be observed. DPC and mineral reactions both take place simultaneously. The grain  
793 size reduction is caused primarily by mineral reaction and nucleation of new  
794 grains. The operation of DPC as a mechanism observed in our experiments  
795 depends on the metastability of minerals in the starting material. This situation is  
796 typical for most basalts and gabbros at amphibolite facies conditions and lower  
797 temperatures.

798 For the continental crust, with its lower geothermal heat gradient compared to the  
799 oceanic crust, mafic fault rocks at common strain rates ( $< 10^{-9} \text{ s}^{-1}$ ) in the presence  
800 of fluids are likely to go through their brittle-viscous transition at much lower  
801 temperatures than observed in our experiments. Hydration reactions of feldspars  
802 at e.g. greenschist facies conditions can lead to grain size reduction and phase  
803 mixing, promoting viscous deformation by grain size sensitive creep mechanisms  
804 (e.g. Fitz Gerald and Stünitz, 1993; Stünitz and Fitz Gerald, 1993).

805 In the oceanic crust, where confining pressures (i.e. lithostatic pressures) are much  
806 lower for same temperatures compared to the continental crust, brittle-viscous  
807 transitional behaviour is likely to occur at higher temperatures, i.e. similar  
808 temperatures like in our experiments (e.g., Mehl and Hirth 2008). As pressures  
809 generally are lower, fracturing is will be more common and is likely contributing to  
810 deformation even to high temperatures.

811 As seen from our experiments, brittle-viscous transitional behaviour is not only a  
812 function of the externally applied parameters such as P and T, but especially a  
813 function of strain, i.e. microstructural evolution. This is an important factor to  
814 consider, as typically rheology of rocks is modelled as a material property without  
815 considering an evolution. We consider that this strain dependent rheology, as  
816 observed in our experiments, can be extrapolated to natural fault systems. Where

817 the strain dependency of rheology bears the potential to lead to a ‘time-dependent’  
818 brittle-viscous transition as microstructure evolves towards favouring viscous  
819 deformation (as seen for the 700 °C experiments in our study).

820

## 821 **5. Summary and conclusions**

822 At the imposed experimental displacement rates, a transition from dominantly  
823 brittle to brittle-viscous to dominantly viscous is observed between the  
824 temperatures 600, 700 and 800 °C. The brittle-viscous transition in our study is  
825 observed to occur via a switch from fracturing to diffusion creep (in the sense of  
826 DPC) and grain boundary sliding as dominant viscous deformation mechanisms.  
827 Viscous deformation in our experiments starts with the onset of diffusive mass  
828 transport and starts to dominate the rheology when fine-grained, interconnected  
829 zones have formed.

830 The important processes enabling viscous rheology are 1) efficient solution-mass  
831 transport, 2) grain size refinement, which in our case as a result of reaction and  
832 nucleation, and 3) shear band interconnection.

833 We observe a brittle-viscous transition not only as a result of increasing  
834 temperatures but also via a microstructural evolution. Especially as the brittle-  
835 viscous transition is approached in terms of temperature (in our case at 700 °C),  
836 more evolved microstructure in shear bands allows for viscous deformation,  
837 whereas low strain lenses still show largely brittle deformation. This leads to a  
838 likely transient, mixed mechanical response of brittle and viscous rheology. For  
839 constant syn-kinematic conditions (i.e. strain rate, P and T, fluid availability, etc.)  
840 the syn-kinematic microstructural evolution with strain (and time) is expected to  
841 change the relative importance of brittle and viscous deformation in favour of the  
842 viscous processes.

843

## 844 **Acknowledgements**

845 We thank the team of the centre of nano imaging (SNI) at Basel University and Tom  
846 Eilertsen at Tromsø University for help and assistance with the electron  
847 microscopy. Terry Tullis is thanked for providing the Maryland Diabase material.  
848 Willy Tschudin is thanked for excellent thin section preparation. We gratefully  
849 acknowledge the funding provided by the Swiss National Foundation grant NF

850 200020\_144448 and financial support from the Freiwillige Akademische  
851 Gesellschaft, Basel, during the last stages of finishing this manuscript.

852

853

854 **References**

855

856 Ashby, M.F., Verrall, R.A., 1973. Diffusion-accommodated Flow and  
857 Superplasticity. *Acta Metallurgica* 21.

858

859 Boullier, A.M., Geugen, Y., 1975. SP-Mylonites: Origin of Some Mylonites by  
860 Superplastic Flow. *Contribution to Mineralogy and Petrology* 50, 93 – 104.

861

862 Brace, W.F., Kohlstedt, D.L., 1980. Limits of Lithospheric Stress Imposed by  
863 Laboratory Experiments. *Journal of Geophysical Research* 85, 6248 – 6252.

864

865 Bukovská, Z., Jerábek, P., Morales, L.F.G., 2016. Major softening at brittle-ductile  
866 transition due to interplay between chemical and deformation processes: An  
867 insight from evolution of shear bands in the South Armorican Shear Zone.  
868 *Journal of Geophysical Research* 121, 1158 – 1182.

869

870 Burov, E.B., 2011. Rheology and strength of the lithosphere. *Marine and*  
871 *Petroleum Geology* 28, 1402–1443.

872

873 Byerlee, J., 1978. Friction of Rocks. *Pure and Applied Geophysics* 116, 615–626.

874

875 Byerlee, J.D., 1968. Brittle-ductile transition in rocks. *Journal of Geophysical*  
876 *Research* 73, 4741 – 4750.

877

878 Byerlee, J.D., 1967. Frictional characteristics of granite under high confining  
879 pressure. *Journal of Geophysical Research* 72, 3639 – 3648.

880

881 Bystricky, M., Mackwell, S., 2001. Creep of dry clinopyroxene aggregates. *Journal*  
882 *of Geophysical Research* 106(B7), 13443 – 13454.

883

884 Carter, N.L., Tsenn, M.C., 1987. Flow properties of continental lithosphere.  
885 *Tectonophysics* 136, 27 – 63.

886

887 Chen, S., Hiraga, T., Kohlstedt, D.L., 2006. Water weakening of clinopyroxene in  
888 the dislocation creep regime. *Journal of Geophysical Research* 111, B08203.

889

890 Coble, R.L., 1963. A Model for Boundary Diffusion Controlled Creep in  
891 Polycrystalline Materials. *Journal of Applied Physics* 34, 1679 – 1682.

892

893 de Ronde, A.A., Stunitz, H., Tullis, J., Heilbronner, R., 2005. Reaction-induced  
894 weakening of plagioclase-olivine composites. *Tectonophysics* 409, 85 – 106.

895

896 Dimanov, A., Dresen, G., 2005. Rheology of synthetic anorthite-diopside  
897 aggregates: Implications for ductile shear zones. *Journal of Geophysical Research*  
898 110, B07203.  
899  
900 Dimanov, A.E., Rybacki, E., Wirth, R., Dresen, G., 2007. Creep and strain-  
901 dependent microstructures of synthetic anorthite-diopside aggregates. *Journal*  
902 *of Structural Geology* 29, 1049 – 1069.  
903  
904 Dimanov, A., Lavie, M.P., Dresen, G., Ingrin, J., Jaoul, O., 2003. Creep of  
905 polycrystalline anorthite and diopside. *Journal of Geophysical Research* 108,  
906 B001815.  
907  
908 Drury, M.R., Avé Lallemant, H.G., Pennock, G.M., Palasse, L.N., 2011. Crystal  
909 preferred orientation in peridotite ultramylonites deformed by grain size  
910 sensitive creep, Étang de Lers, Pyrenees, France. *Journal of Structural Geology*  
911 33, 1776 – 1789.  
912  
913 Drury, M.R., Humphreys, F., 1988. Microstructural shear criteria associated with  
914 grain-boundary sliding during ductile deformation. *Journal of Structural Geology*  
915 10, 83 – 89.  
916  
917 Elliott, D., 1973. Diffusion Flow Laws in Metamorphic Rocks. *Geological Society of*  
918 *America Bulletin* 84, 2645–2664.  
919  
920 Fitz Gerald, J.D., Boland, J.N., McLaren, A.C., Ord, A., Hobbs, B., 1991.  
921 Microstructures in water-weakened single crystals of quartz. *Journal of*  
922 *Geophysical Research* 96, 2139 – 2155.  
923  
924 Fitz Gerald, J.D., Stünitz, H., 1993. Deformation of Granitoids at low Metamorphic  
925 Grade. 1. Reactions and Grain-size Reduction. *Tectonophysics* 221, 269–297.  
926  
927 Fossen, H., Tikoff, B., 1993. The deformation matrix for simultaneous simple  
928 shearing, pure shearing and volume change, and its application to transpression-  
929 transtension tectonics. *Journal of Structural Geology* 15, 413 – 422.  
930  
931 Fousseis, F., Handy, M.R., 2008. Micromechanisms of shear zone propagation at  
932 the brittle–viscous transition. *Journal of Structural Geology* 30, 1242–1253.  
933  
934 Gerbi, C., Johnson, S.E., Shulman, D., Klepeis, K., 2016. Influence of microscale  
935 weak zones on bulk strength. *Geochemistry Geophysics Geosystems* 17, 4064 –  
936 4077.  
937  
938 Getsinger, A.J., Hirth, G., 2014. Amphibole fabric formation during diffusion creep  
939 and the rheology of shear zones. *Geology* 42, 535 – 538.  
940  
941 Gifkins, R.C., 1976. Grain-Boundary Sliding and its Accommodation During Creep  
942 and Superplasticity. *Metallurgical Transactions* 7A, 1225 – 1232.  
943

944 Goldsby, D., Tullis, T.E., 2002. Low frictional strength of quartz rocks at  
945 subseismic slip rates. *Geophysical Research Letters* 29, L015240.  
946  
947 Goncalves, P., Poilvet, J.-C., Oliot, E., Trap, P., 2016. How does shear zone  
948 nucleate? An example from the Suretta nappe (Swiss Eastern Alps). *Journal of*  
949 *Structural Geology* 86, 166 – 180.  
950  
951 Gratier, J.-P., Dysthe, D.K., Francois, R., 2013. The Role of Pressure Solution Creep  
952 in the Ductility of the Earth's Upper Crust, in: Dmowska, R. (Ed.), *Advances in*  
953 *Geophysics*. pp. 47 – 179.  
954  
955 Gratier, J.-P., Guiguet, R., Renard, F., Jenatton, L., Bernard, D., 2009. A pressure  
956 solution creep law for quartz from indentation experiments. *Journal of*  
957 *Geophysical Research* 114, B03403.  
958  
959 Gratier, J.-P., Richard, J., Renard, F., Mittempergher, S., Doan, M.-L., Di Toro, G.,  
960 Hadizadeh, J., Boullier, A.-M., 2011. Aseismic sliding of active faults by pressure  
961 solution creep: Evidence from the San Andreas Fault Observatory at Depth.  
962 *Geology* 39, 1131–1134.  
963  
964 Green, H. W. II, Borch, R. S., 1989. A new molten salt cell for precision stress  
965 measurements at high pressure. *Eur. J. Miner.* 1, 213 - 219.  
966  
967 Griggs, D.T., Turner, F.J., Heard, H.C., 1960. Deformation of rocks at 500 to 800°C.  
968 *Geol. Soc. Am., Mem.* 79, 39 – 105.  
969  
970 Hacker, B.R., Christire, J.M., 1991. Experimental deformation of a glassy basalt.  
971 *Tectonophysics* 200, 79 – 96.  
972  
973 Handin, J., 1966. Strength and ductility, in: Clark, S.P. (Ed.), *Handbook of Physical*  
974 *Constants*, *Geol. Soc. Am. Mem.* pp. 223 – 289.  
975  
976 Hawthorne, F. C., Oberti, R., Harlow, G. E., Maresch, W. V., Martin, R. F.,  
977 Schumacher, J. C., and Welch, M. D., 2012. Nomenclature of the amphibole  
978 supergroup. *American Mineralogist* 97, 2031 – 2048  
979  
980 Heard, H.C., 1960. , in: Griggs, D.T., Handin, J. (Eds.), *Transition from Brittle*  
981 *Fracture to Ductile Flow in Solnhofen Limestone as a Function of Temperature,*  
982 *Confining Pressure and Interstitial Fluid Pressure, Rock Deformation, Mem. Geol.*  
983 *Soc. Am. New York*, pp. 193 – 226.  
984  
985 Heilbronner, R., Barrett, S., 2014. *Image Analysis in Earth Sciences -*  
986 *Microstructures and Textures of Earth Materials.* Springer-Verlag, Berlin.  
987  
988 Holyoke III, C.W., Kronenberg, A.K., 2010. Accurate differential stress  
989 measurement using the molten salt cell and solid salt assemblies in the Griggs  
990 apparatus with applications to strength, piezometers and rheology.  
991 *Tectonophysics* 494, 17 – 31.

992 Janssen, C., Wirth, R., Rybacki, E., Naumann, R., Kemnitz, H., Wenk, H.-R., Dresen,  
 993 G., 2010. Amorphous material in SAFOD core samples (San Andreas Fault):  
 994 Evidence for crush-origin pseudotachylytes? *Geophysical Research Letters* 37,  
 995 L01303.  
 996  
 997 Karato, S.-I., 2008. *Deformation of Earth Materials - an introduction to the*  
 998 *rheology of solid earth*. Cambridge University Press, Cambridge.  
 999  
 1000 Keulen, N., Heilbronner, R., Stünitz, H., Boullier, A.-M., Ito, H., 2007. Grain size  
 1001 distributions of fault rocks: A comparison between experimentally and naturally  
 1002 deformed granitoids. *Journal of Structural Geology* 29, 1282 – 1300.  
 1003  
 1004 Kilian, R., Heilbronner, R., Stünitz, H., 2011. Quartz grain size reduction in a  
 1005 granitoid rock and the transition from dislocation to diffusion creep. *Journal of*  
 1006 *Structural Geology* 33, 1265–1284.  
 1007  
 1008 Kohlstedt, D.L., Evans, B., Mackwell, S.J., 1995. Strength of the Lithosphere:  
 1009 Constraints imposed by laboratory experiments. *Journal of Geophysical Research*  
 1010 100 (17), 517–587  
  
 1011 Kohlstedt, D.L., Hansen, L.N., 2015. Constitutive equations, rheological behavior,  
 1012 and viscosity of rocks, in: Schubert, G. (Ed.), *Treatise on Geophysics*. Elsevier,  
 1013 Oxford, pp. 441 – 472.  
 1014  
 1015 Kronenberg, A.K., Shelton, G.L., 1980. Deformation microstructures in  
 1016 experimentally deformed Maryland Diabase. *Journal of Structural Geology* 2, 341  
 1017 – 353.  
 1018  
 1019 Mackwell, S.J., 1991. High-temperature creep of enstatite single crystals.  
 1020 *Geophysical Research Letters* 18, 2027 – 2030.  
 1021  
 1022 Mancktelow, N.S., Pennacchioni, G., 2005. The control of precursor brittle  
 1023 fracture and fluid–rock interaction on the development of single and paired  
 1024 ductile shear zones. *Journal of Structural Geology* 27, 645 – 661.  
 1025  
 1026 Panozzo Heilbronner, R., 1984. Two-dimensional strain from the orientation of  
 1027 lines in a plane. *Journal of Structural Geology* 6, 215 – 221.  
 1028  
 1029 Paterson, M.S., 2013. *Materials Science for Structural Geology*. Springer,  
 1030 Dordrecht.  
 1031  
 1032 Paterson, M.S., Wong, T.-F., 2005. *Experimental Rock Deformation – The Brittle*  
 1033 *Field*, 2nd ed. Springer, Berlin Heidelberg.  
 1034  
 1035 Pec, M., Stünitz, H., Heilbronner, R., Drury, M., 2016. Semi-brittle flow of granitoid  
 1036 fault rocks in experiments. *Journal of Geophysical Research Solid Earth* 121,  
 1037 B012513.  
 1038

1039 Pec, M., Stünitz, H., Heilbronner, R., Drury, M., de Capitani, C., 2012. Origin of  
1040 pseudotachylites in slow creep experiments. *Earth and Planetary Science Letters*  
1041 355-356, 299 – 310.  
1042  
1043 Pennacchioni, G., Mancktelow, N., 2007. Nucleation and initial growth of a shear  
1044 zone network within compositionally and structurally heterogeneous granitoids  
1045 under amphibolite facies conditions. *Journal of Structural Geology* 29, 1757–  
1046 1780.  
1047  
1048 Price, N.A., Johnson, S.E., Gerbi, C.C., West Jr., D.P., 2012. Identifying deformed  
1049 pseudotachylyte and its influence on the strength and evolution of a crustal  
1050 shear zone at the base of the seismogenic zone. *Tectonophysics* 518-521, 63 s  
1051 518  
1052  
1053 Raterron, P., Jaoul, O., 1991. High-temperature deformation of diopside single  
1054 crystal, 1. mechanical data. *Journal of Geophysical Research* 96, 14277 – 14286.  
1055  
1056 Richter, B., Stünitz, H., Heilbronner, R., 2016. Stresses and pressures at the  
1057 quartz-to-coesite phase transformation in shear- deformation experiments.  
1058 *Journal of Geophysical Research Solid Earth* 121, B013084.  
1059  
1060 Rutter, E.H., 1976. The kinetics of rock deformation by pressure solution.  
1061 *Philosophical Transactions of the Royal Society of London* 283, 203 – 219.  
1062  
1063 Rutter, E.H., Peach, C.J., White, S.H., Johnston, D., 1985. Experimental  
1064 “syntectonic” hydration of basalt. *Journal of Structural Geology* 7, 251 – 266.  
1065  
1066 Rybacki, E., Dresen, G., 2000. Dislocation and diffusion creep of synthetic  
1067 anorthite aggregates. *Journal of Geophysical Research* 105, 26017 – 26036.  
1068  
1069 Rybacki, E., Gottschalk, M., Wirth, R., Dresen, G., 2006. Influence of water fugacity  
1070 and activation volume on the flow properties of fine-grained anorthite  
1071 aggregates. *Journal of Geophysical Research* 111, B03203.  
1072  
1073 Schmid, S., Panozzo, R., Bauer, S., 1987. Simple shear experiments on calcite  
1074 rocks: rheology and microfabric. *Journal of Structural Geology* 9, 747 – 778.  
1075  
1076 Shelton, G., Tullis, J., Tullis, T., 1981. Experimental high temperature and high  
1077 pressure faults. *Geophysical Research Letters* 8, 55 – 58.  
1078  
1079 Sibson, R.H., 1984. Roughness at the Base of the Seismogenic Zone: Contributing  
1080 Factors. *Journal of Geophysical Research* 89, 5791 – 5799.  
1081  
1082 Sibson, R.H., 1982. Fault zone models, heat flow, and the depth distribution of  
1083 earthquakes in the continental crust of the United States. *Bulletin of the*  
1084 *Seismological Society of America* 72, 151 – 163.  
1085  
1086 Simpson, C., 1986. Fabric Development in Brittle-to-Ductile Shear Zones. *Pure*  
1087 *and Applied Geophysics* 124, 269–288.



1088  
1089 Stel, H., 1981. Crystal growth in cataclasites: Diagnostic microstructures and  
1090 implications. *Tectonophysics* 78, 585 – 600.  
1091  
1092 Storti, F., Billi, A., Salvini, F., 2003. Particle size distributions in natural carbonate  
1093 fault rocks: insights for non-self-similar cataclasis. *Earth and Planetary Science*  
1094 *Letters* 206, 173 – 186.  
1095  
1096 Stünitz, H., Fitz Gerald, J.D., 1993. Deformation of granitoids at low metamorphic  
1097 grade. II: Granular flow in albite-rich mylonites. *Tectonophysics* 221, 229 – 324.  
1098  
1099 Trepmann, C.A., Stöckert, B., 2003. Quartz microstructures developed during  
1100 non-steady state plastic flow at rapidly decaying stress and strain rate. *Journal of*  
1101 *Structural Geology* 25, 2035 – 2051.  
1102  
1103 Tullis, J., Yund, A., 1987. Transition from cataclastic flow to dislocation creep of  
1104 feldspar: Mechanisms and microstructures. *Geology* 15, 606 – 609.  
1105  
1106 Tullis, J., Yund, R.A., 1977. Experimental deformation of dry Westerly granite.  
1107 *Journal of Geophysical Research* 82, 5705 – 5718.  
1108  
1109 Yund, R.A., Blanpied, M.L., Tullis, T.E., Weeks, J.D., 1990. Amorphous material in  
1110 high strain experimental fault gauges. *Journal of Geophysical Research* 95, 15589  
1111 – 15602.  
1112  
1113  
1114  
1115  
1116  
1117  
1118  
1119

1120 **Figure Captions**

1121

1122 **Figure 1** : Sample assembly. a) Schematic cross-section of sample assembly. Inset  
1123 shows details on sample. b) Thin section of sample 449 after deformation. Black  
1124 arrow indicates unloading crack. FB = forcing block, SZ = shear zone.

1125

1126 **Figure 2** : Reference frame and definitions. a) Micrographs are oriented with the  
1127 shear zone boundaries parallel to the x-direction with a dextral sense of shear. b)  
1128 In rose diagrams, preferred orientations are marked with black dots;  $\theta$  = angle  
1129 between orientation and applied load ( $\sigma_1$  direction);  $\Phi$  = angle between  
1130 orientation and shear plane (shear zone boundaries). c) Stresses are plotted as  
1131 shear stress  $\tau$  versus apparent shear strain  $\gamma_a$ , see Appendix. Stages of the  
1132 experiment are indicated.

1133

1134 **Figure 3** : Mechanical data. a) Shear stress vs. apparent shear strain for  
1135 experiments performed at  $T = 600, 700$  and  $800$  °C, using confining pressures  
1136 ( $P_c$ ) of  $\sim 0.5, 1.0$  and  $1.5$  GPa. Shear strain rate for all experiments is  $\sim 3 \times 10^{-5} s^{-1}$ . b) Mohr diagrams for same experiments.  $\sigma_3$  = confining pressure;  $\sigma_1$  = yield  
1137 stress. (black lines) or quasi-steady state (grey dotted lines). In red, apparent  
1138 friction coefficient  $\mu'$  and angle of internal friction.  $\mu'$  values decrease with  
1139 increasing  $T$  and increasing  $P_c$ . Stress values usually stay below Byerlees  
1140 relationship except for  $600$  and  $700$  °C experiments at  $P_c = 0.5$  GPa.

1142

1143 **Figure 4** : Derivation of stress exponents. a) Shear stress vs. apparent shear strain  
1144 rate, with calculated stress exponent  $n$ ; slope of linear fit is  $1/n$ . b) Different stress  
1145 exponents calculated for different data-correction routines shown for two  
1146 experiments performed at  $T = 800$  °C /  $P_c = 1.0$  GPa and  $T = 300$  °C /  $P_c = 0.5$ GPa.  
1147 R16 = after Richter et al., 2016; H&K10 = after Holyoke & Kronenberg, 2010; P12=  
1148 after Pec et al, 2012 (see Methods).

1149

1150 **Figure 5** : Microstructure development across the brittle-viscous transition.  
1151 Experimental conditions are indicated, dextral shear sense applies to all. a) and  
1152 b) At  $T = 600$  °C, fracturing is extensive; a foliation (S) is developed by cataclastic

1153 flow; shear displacement is accommodated along shear bands and shear  
1154 fractures in Riedel shear (R) orientations. c) Pore trails along fractures indicate  
1155 partial healing. d) and e) At T=700 °C, fracturing is extensive in Px  
1156 porphyroclasts; a foliation (S) is developed partly by cataclastic flow. e) Shear  
1157 bands are recognized by a fine-scale compositional layering and intense grain  
1158 size reduction; hydrous reaction products Amph and Zo are beginning to form. f)  
1159 and g) At T = 800 °C, broad shear bands (white stippled lines) anastomose  
1160 around low strain lenses; they are characterized by grain size reduction and the  
1161 formation of a foliation parallel to the shear band boundaries; hydrous reactions  
1162 products Amph and (to a lower extent) Zo are formed.

1163

1164 **Figure 6 :** Hydrous reactions at 700 °C. Left: digitally produced phase maps,  
1165 right, BSE image of the same area. Dark grey = Pl; orange = Amph; bright grey =  
1166 Px ; sample deformed at T = 700 °C, Pc = 1.0 GPa. Amph follows zones of high  
1167 strain such as shear bands, or fractures within Px clasts.

1168

1169 **Figure 7 :** Shear band morphology as a function of temperature. Shear bands  
1170 and shear fractures are traced in red. Light background layer are BSE contrast  
1171 images of the shear zones. Rose diagrams (surface ODFs) show orientation of  
1172 boundary segments of the traced structures. Horizontal shear bands developed  
1173 at the forcing block-shear zone interface are omitted from the analysis. Rose  
1174 diagrams show the dominance of more shear zone parallel shear bands at higher  
1175 experimental T. b) Shear band width distributions. Shear bands stay largely  
1176 below 10 µm at 600 °C, and get broader at higher T, reaching up to 70 µm for the  
1177 presented 800 °C experiment.

1178

1179 **Figure 8 :** Micro- to nanostructures of shear bands developed at 600 °C. a) SEM  
1180 BSE image of a shear band formed in the sample near interface with the forcing  
1181 block; shear sense is dextral. b) - d) TEM images of a shear band similar to the  
1182 one shown in a). Kinematic reference frame for images b) - d) is given in upper  
1183 right corner in b). b) BF TEM image. Increasing grain size refinement from top to  
1184 lower half of the image; cryst = crystalline; amor = amorphous. Note few  
1185 remaining crystals (darker) within amorphous layers. c) HAADF (left) and BF

1186 TEM image (right) of nano-crystals mainly formed by Px; amorphous layers  
1187 correlate with the typical darker grey-value of Pl. d) High-resolution BF image  
1188 from a central part of the shear band; nano-crystalline layer enclosed between  
1189 amorphous domains. White squares denote areas where diffraction spots are  
1190 detected in FFT analyses (see Methods); locally, amorphous layers contain nano-  
1191 crystals, identified both from diffraction spots in FFT images and from their dark  
1192 appearance in the BF image.

1193

1194 **Figure 9** : Micro- to nanostructures of shear bands developed at 700 °C. a) SEM  
1195 BSE image of a shear band. b) SE SEM image of the surface of a shear band;  
1196 mostly Pl grains are visible; white arrow indicates shear direction, with top to  
1197 the upper right. c) HAADF image showing a Px porphyroclast adjacent to a fine  
1198 grained shear band formed by Pl + Amph; the Px porphyroclast shows a thin  
1199 reaction corona of Amph; black arrow points to porosity within the Px clast. d)  
1200 HAADF image of a Pl porphyroclast with surrounding fine-grained Pl in a shear  
1201 band; the trace of an EDS profile is marked. Kinematic reference frame is the  
1202 same as in c). e) Element counts of Si, Ca and Al (normalized to max. count value  
1203 of the respective element) versus distance (pixel) along the profile marked in d);  
1204 mean values (blue) are indicated for the porphyroclast and the Pl of the shear  
1205 band.

1206

1207 **Figure 10** : Micro- to nanostructures of shear bands developed at 800 °C. a) SE  
1208 BSE image of a shear band with typical compositional layering of Pl dominated  
1209 layers alternating with Amph+Qz(+Pl) mixed layers. b) BF TEM image of Pl  
1210 grains within a shear band; grains show a low defect density; porosity is low and  
1211 grain boundaries are tight. c) HAADF image showing the typical compositional  
1212 layering of Pl dominated layers alternating with Amph+Qz aggregates. d) BF-  
1213 STEM image of the same area as in c).

1214

1215 **Figure 11** : Shape of plagioclase grains in shear bands at 800 ° C. a) BF TEM  
1216 image of diamond-shaped Pl grains with a weak shape preferred orientation. b)  
1217 Rose diagram (surface ODF) of Pl grain boundaries preferentially oriented at  $\Phi$   
1218 = 10-30° . The ODF shows a weak anisotropy consistent with the dextral sense

1219 of shear. c) Grain boundary segments are visualized separately for horizontal (-  
1220  $30^\circ < \Phi < 30^\circ$ ) and vertical ( $30^\circ < \Phi < 150^\circ$ ) orientations (marked black in rose  
1221 diagrams).

1222

1223 **Figure 12** : Grain size distribution of plagioclase in shear bands. a) Sample 416  
1224 deformed at  $T = 700^\circ\text{C}$ ,  $P_c = 1.0\text{ GPa}$ ; area equivalent grain diameters,  $d_{\text{equ}}$ , were  
1225 determined from SE images as shown in Fig. 9b. b) Sample 414 deformed at  $T =$   
1226  $800^\circ\text{C}$ ,  $P_c = 1.0\text{ GPa}$ ; area equivalent grain diameters,  $d_{\text{equ}}$ , were determined  
1227 from TEM images of the FIB-foil shown in Fig. 10. Dark grey bars represent  
1228  $>80\%$  of all grains; black line = kernel density estimate fit, number of grains,  $n$ ,  
1229 and mode of curve fit are indicated.

1230

1231 **Figure 13** : Evolution of shear bands with increasing strain. a) Central parts of  
1232 shear zones deformed at  $T = 800^\circ\text{C}$  and  $P_c = 1.0\text{ GPa}$  to increasing apparent  
1233 shear strains; sample 449 ( $P_c = 1.5\text{ GPa}$ ) is included for comparison. Shear bands  
1234 are shown in orange; rose diagrams with surface ODF of shear band boundary  
1235 segments on right. With increasing strain, dominant shear band orientation  
1236 becomes more shear zone parallel and shear bands become wider and better  
1237 interconnected. b) Stress - strain curves for samples shown in a). c) Increase of  
1238 area fraction of shear bands with increasing shear strain. Although geometry of  
1239 shear bands at 1.0 and 1.5 GPa differ, their area-% is identical..

1240

1241 **Figure 14** : Zones of initial shear localization. BSE SEM image of sample 460  
1242 deformed at  $T = 800^\circ\text{C}$ ,  $P_c = 1.0\text{ GPa}$ . Black arrows point to minute segregation  
1243 of melt; nucleation of new Amph (white arrow) and Pl grains is observed.

1244

1245 **Figure 15** : Comparison of shear band orientation formed at peak stress (left)  
1246 and at higher strains at quasi steady state. Rose diagrams are surface ODFs of  
1247 shear zone boundary segments. Initiation of shear band shows comparable  
1248 preferred angles for all temperatures. At higher temperatures however, shear  
1249 band orientations are more shear zone parallel with increasing strain, i.e.  
1250 microstructural evolution.

1251

1252 **Table 1** : Composition of Maryland Diabase starting material. EDS  
1253 measurements as oxide wt.-% and calculated to stoichiometric mineral formula.  
1254

1255 **Table 2** : List of experiments and experimental conditions.

1256 T = Temperature

1257 Pc = Confining pressure, averaged between  $\gamma_a = 1.5$  to end of experiment;

1258 (\*) denotes peak stress experiments where average Pc is calculated between  
1259 beginning and end of experiment.

1260 Peak  $\tau$  = Maximum shear stress.

1261 Flow  $\tau$  = Shear stress during quasi-steady state or at end of experiment.

1262  $\gamma_a$  = Total apparent shear strain.

1263  $\dot{\gamma}_a$  = Apparent shear strain rate: (1) constant displacement rate

1264 experiments.  $\dot{\gamma}_a$  calculated as the average value between  $\gamma_a = 1.5$  and end

1265 of experiment; (2) displacement rate stepping tests.  $\dot{\gamma}_a$  as average value

1266 for each setting.

1267

1268 **Appendix Figure 1** : General shear setup within initial state and shear zone

1269 thickness, th0, and state at end of experiment and final shear zone thickness, thF.

1270 For representation purposes, the displacement is displayed to occur asymmetric

1271 by shift of only the upper forcing block.

1272 **Appendix Table 1** : Different measures for shear strain.

1273 th0 = estimated shear zone thickness at start of experiment (Appendix Figure 2).

1274 thF = measured shear zone thickness at end of experiment (Appendix Figure 1).

1275 d = axial displacement of  $\sigma_1$ -piston.

1276 sdF = displacement of  $\sigma_1$ -piston parallel to shear zone boundary (Appendix  
1277 Figure 1).

1278  $k = th0/thF$  = pure shear component.

1279  $thF/th0$  (%) = relative thickness of sample after deformation.

1280  $\Gamma_{eff}$  = effective shear strain (Appendix Eq. (A4)).

1281  $\gamma_{TH}$  = shear strain determined from relative displacement of forcing blocks as  
1282 measured on thin sections.

1283  $\gamma_{\text{comp}}$  = simple shear component (Appendix Eq. (A5)).  
 1284  $\gamma_{\text{a}}$  = apparent shear strain (Appendix Eq. (A2)).  
 1285  $R_f$  = aspect ratio of finite strain ellipse (after Fossen & Tikoff, 1973).  
 1286  $\phi$  = orientation of finite stretching direction (after Fossen and Tikoff, 1973).  
 1287  $\varepsilon_{\text{m}}$  = strain magnitude (Appendix Eq. (A6)).

1288  
 1289

## 1290 **Appendix**

### 1291 *A1. Derivation of shear strains*

1292 General shear experiments like the ones described in this paper often experience  
 1293 sample thinning, even if the samples are pre-compacted or annealed before the  
 1294 actual start of the shear deformation. Thinning continues throughout the  
 1295 experiments, as inferred from samples deformed under identical conditions to  
 1296 different total strains. It is usually observed that the sample material does not  
 1297 escape sideways. The strain is therefore taken to be plane strain and calculations  
 1298 are made in 2 dimensions by assuming a combination of pure shear (thinning of  
 1299 shear zone) and simple shear (displacement parallel to the piston-sample  
 1300 interface).

1301 Measurements indicate that the samples thin linearly from the beginning of the  
 1302 experiment to the end. Correlating the shear zone thickness,  $thF$ , with the axial  
 1303 displacement,  $d$ , a linear trend of shear zone thinning is evident ([Appendix Figure](#)  
 1304 [1](#)). The initial thickness, i.e., the thickness of the compacted samples at the start of  
 1305 the experiment, depends on temperature. Two initial thicknesses for  $T = 800^\circ\text{C}$  and  
 1306  $T \leq 700^\circ\text{C}$  are derived ([Appendix Table 1](#)).

1307 For strain calculations, the axial displacement,  $d$ , of the  $\sigma_1$ -piston is partitioned  
 1308 into a shear component parallel to the  $45^\circ$  sample piston interface, and a thinning  
 1309 component normal to the shear zone boundary. Dividing the total shear  
 1310 displacement  $sdF$ , by the final thickness  $thF$ ,  $\gamma_{\text{TH}}$  is derived ([Appendix Figure 2](#)).

1311

$$1312 \quad \gamma_{\text{TH}} = sdF / thF \quad (A1a)$$

$$1313 \quad sdF = (d - (th_0 - thF) \cdot \cos(45^\circ)) / \cos(45^\circ) \quad (A1b)$$

1314

1315 where:  $sdF$ : total displacement parallel to the piston-sample interface;  $th0 / thF$ :  
 1316 initial / final thickness of sample.

1317 In this study, the shear strain is calculated from the experimental record as the  
 1318 sum of individual increments of shear displacement divided by the instantaneous  
 1319 shear zone thickness. The shear strain derived in this manner is referred to as  
 1320 apparent shear strain  $\gamma_a$ :

1321

$$1322 \quad \gamma_a(k) = \sum_{i=2}^k \frac{sd(i) - sd(i-1)}{th(i)} \quad (A2)$$

1323

1324  $sd(i)$  : displacement along piston-sample interface;  $th(i)$  : shear zone thickness at  
 1325 time  $i$ . The shear strain values calculated in this fashion depend on the thinning of  
 1326 the sample.  $\gamma_a$  is termed 'apparent', as it is not a real measure of simple shear.

1327 The pure shear component of the sample strain is calculated as

1328

$$1329 \quad k = th0 / thF \quad (A3)$$

1330

1331 Following Fossen and Tikoff (1993), the effective shear strain,  $\Gamma_{eff}$ , and the simple  
 1332 shear strain component,  $\gamma_{comp}$ , are derived as

1333

$$1334 \quad \Gamma_{eff} = k^{-1} \cdot \tan(\psi) = sdF / th0 \quad (A4)$$

1335

$$1336 \quad \gamma_{comp} = \Gamma_{eff} \cdot \frac{2 \ln(k)}{k - k^{-1}} \quad (A5)$$

1337

1338 The difference between the strain measures is small as shown in [Appendix Figure](#)  
 1339 [3](#). Note that, if  $thF = th0$ , i.e., if  $k = 1$ , all strain measures coincide:  $\gamma_{TH} = \gamma_a = \Gamma =$   
 1340  $\gamma_{comp}$ . In order to be able to convert from axial to shearing experiments, the strain  
 1341 magnitude is derived after Schmid et al. (1987):

1342

$$1343 \quad \varepsilon_m = \frac{1}{\sqrt{3}} [(\varepsilon_1 - \varepsilon_2)^2 + (\varepsilon_2 - \varepsilon_3)^2 + (\varepsilon_3 - \varepsilon_1)^2]^{1/2} \quad (A6)$$

1344



1345 where  $\varepsilon_m$  = strain magnitude;  $\varepsilon_1, \varepsilon_2, \varepsilon_3$  = axes of the strain ellipsoid calculated  
1346 after Fossen and Tikoff (1993). Plane strain conditions are assumed with  $\varepsilon_2 = 1$ .  
1347  
1348